

Bubble nucleation in rhyolitic melts: Experiments at high pressure, temperature, and water content

Shaul Hurwitz, Oded Navon

Institute of Earth Sciences, The Hebrew University, Jerusalem 91904, Israel

(Received September 21, 1993; revision accepted February 23, 1994)

Abstract

We report the first measurement of bubble nucleation in hydrated rhyolitic melts in response to pressure release. Two rhyolitic obsidians, one containing less than 1% of microlites of Fe-Ti oxides and the other about 20% of various crystals were hydrated at 150 MPa and 780–850°C. After saturation was reached (5.3–5.5 wt% water), pressure was lowered and the samples were allowed to nucleate and grow bubbles for various amounts of time, before the final, rapid quenching of the experiments.

The results demonstrate the importance of heterogeneous nucleation. Microlites of Fe-Ti oxides are very efficient as sites for bubble nucleation. In their presence, modest nucleation was observed even after decompression by < 1 MPa, and decompression of more than 5 MPa produced extensive nucleation (10^6 – 10^8 bubbles cm^{-3}). In the absence of microlites, no nucleation occurred at $\Delta P < 10$ MPa. At $\Delta P > 10$ MPa, bubbles also nucleated on crystals of biotite, zircon and apatite. Modest nucleation (10^3 – 10^5 cm^{-3}) took place even in crystal-free samples, but it was still heterogeneous. When ΔP exceeded 80 MPa, nucleation in crystal-free samples became extensive (10^5 – 10^7 cm^{-3}). The lack of correlation of bubble density with either time or decompression suggests that nucleation was still heterogeneous. Nucleation rates were controlled mainly by the availability of sites. Rates were faster than 10^6 cm^{-3} s^{-1} when microlites were present, and faster than 10^5 cm^{-3} s^{-1} in the absence of microlites at $\Delta P > 70$ MPa. Narrow size distributions in most samples suggests that nucleation took place immediately after the pressure drop.

The experimental data we present here indicate that the presence or absence of efficient nucleation sites can lead to two distinct modes of bubble formation. When a large number of efficient sites (e.g., Fe-Ti oxide) are present, bubble nucleation requires very little supersaturation, and to a good approximation, gas and magma are in equilibrium. In magmas that are crystal-free or contain crystals that are inefficient at nucleating bubbles, very high degrees of supersaturation are required in order to initiate nucleation. These two modes of exsolution may lead to contrasting styles of convection, pressure build up and eruption.

1. Introduction

Silicic volcanism in island arcs, continental margins and intraplate settings is commonly characterized by violent explosive eruptions. The ex-

plosive nature of the volcanism is largely due to exsolution of volatiles dissolved in these viscous magmas. The well-accepted general model of eruption [1,2] assumes a shallow magma chamber with magma that is saturated, or slightly undersaturated in volatiles. Pressure release, heating, or crystallization may lead to supersaturation, and when a critical level of supersaturation is

[CL]

attained, bubbles nucleate. The bubbles grow by diffusion of volatiles from the melt and by response to pressure release. When the gas volume approaches 75–80% of the gas–melt mixture, fragmentation of the melt occurs [3,4]. In the case of rhyolites, the major dissolved volatile is water; other volatiles (e.g., CO_2 , SO_2 , HF and HCl) occur in much lower concentrations [5–7].

The nucleation of bubbles is a key process in controlling the nature of an eruption, although until recently this subject has surprisingly received only little attention. Sparks' comprehensive work [3] summarizes all previous models, and has pointed out that, according to classical nucleation theory [8], the high surface tension of water bubbles in rhyolitic melts should prevent the nucleation of bubbles until extremely high values of supersaturation are attained. In spite of this, only homogeneous nucleation was considered in later studies [9,10]. Toramaru [11] and Mangan et al. [12] tried to deduce nucleation rates from studies of bubble size distribution in natural andesites and basalts, again assuming homogeneous nucleation. Heterogeneous nucleation has been reviewed in the engineering literature [13–16]. Experimental studies of the nucleation process in natural melts were attempted only by Murase and McBirney [17], and more recently by Bagdassarov and Dingwell [18], who noted that nucleation rates increased by more than an order of magni-

tude when micrometre-size crystals of ore minerals were present in the starting material. In both cases, the starting materials were natural obsidians with low water contents ($> 0.5\%$), and bubble nucleation was initiated by heating the sample at room pressure, and decreasing the solubility of water in the melt. Here we report the result of an experimental study of homogeneous and heterogeneous nucleation of water bubbles in hydrated natural rhyolite. The driving force for nucleation is a rapid decrease in the confining pressure, and the experiments were carried out under geologically relevant temperatures, pressures and water contents.

2. Experimental method

Rhyolitic obsidian from Little Glass Butte (LGB), Oregon and from South Deadman Creek (SDC), the Inyo craters, California were used as starting materials. The LGB material consists of clear, colourless glass that contains less than 1 vol% microlites of Fe-oxides concentrated along flow bands (Fig. 1a). The microlites are large (about 2–5 μm in size) and connected by narrow, string-like Fe-oxides. Rare feldspars are also present. SDC rhyolite (Fig. 1b) contains about 20% crystals, including plagioclase, biotite, K-feldspar, apatite, Fe-Ti oxides, and rare amphibole and

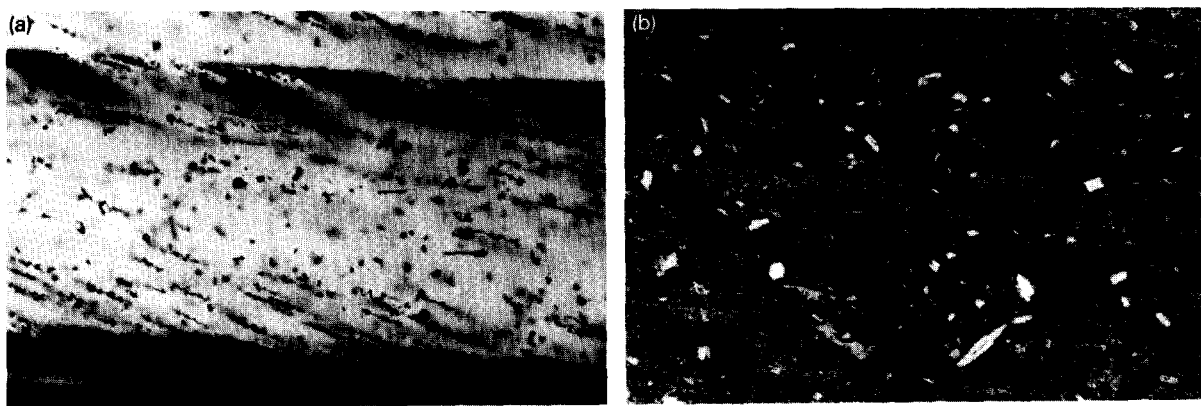


Fig. 1. Starting materials. (a) Rhyolitic obsidian from Little Glass Butte (LGB), Oregon. The darker regions carry a high concentration of microlites of Fe-oxides (length of photograph = 420 μm). (b) Rhyolitic obsidian from South Deadman Creek (SDC), Inyo Craters, California (polarizers at 60° , length of photograph = 420 μm).

quartz. Bulk analyses of LGB and SDC rhyolites, and an electron microprobe analysis of the crystal-free regions, are listed in Table 1.

Sawn slabs ($1 \times 4 \times 8$ mm) of natural rhyolite were cleaned with hydrochloric acid and deionized water and then loaded in gold capsules together with more than 10 wt% double-distilled water. The capsules were then sealed and loaded into cold-seal pressure vessels made of RENE alloy and designed to allow rapid quenching of the experiments [19].

Initial experiments at 150 MPa and 800°C have shown that homogeneously hydrated glass is produced after 3 days, in agreement with diffusion calculations (using the coefficients of Zhang et al. [20]). All samples were hydrated at 150 MPa at temperatures of between 780 and 850°C. Run durations varied between 3 and 7 days, with most of the low-temperature runs lasting more than 4 days. After hydration, pressure was dropped and held at the new lower value for variable amounts of time, allowing the supersaturated melt to exsolve its excess water. It commonly took about 3–5 s to release pressure by a few tens of megapascals, and 5–10 s to drop the pressure by more than 100 MPa. At the end of the experiments, the samples were dropped into the water-cooled lower part of the pressure vessel, where they cooled

under pressure to room temperature in less than 2 s. Quenching caused a few megapascals increase in pressure.

Pressure was measured using a Heise pressure gauge with an accuracy of < 1 MPa. Pressure fluctuations due to daily variations in room temperature were up to 1 MPa. Temperature was controlled by a Eurotherm 808 controller to $\pm 1^\circ\text{C}$, using an external thermocouple. Temperatures at the sample location inside the vessels were determined to be higher than the readings of the external thermocouple and were corrected accordingly (3°C at 780–800°C, 4°C at 850°C). Temperature differences between the top and bottom of the sample were less than 2°C , except for samples LGB-10, 17, 24, 35 and 58 where they reached 5°C .

At the end of the run, the capsules were opened and the obsidian was polished. Water content was determined spectroscopically on selected samples using a NICOLET 740 FTIR and the calibration of Newman et al. [21] and Ihinger [19]. Samples hydrated at 850°C contain about 5.3 wt% H_2O , in agreement with solubility data [19,22]. Samples hydrated at 800°C contain 5.5 wt%. The size and number density of the bubbles that grew during the experiments were determined either directly under a Nikon petrographic

Table 1
Chemical analysis of starting material

oxide	LGB		SDC	
	glass ⁽¹⁾	bulk ⁽²⁾	glass	bulk
SiO_2	76.92	77.03	69.71	69.92
TiO_2	n.d. ⁽³⁾	0.08	0.27	0.24
Al_2O_3	12.23	12.46	15.68	16.28
$\text{FeO}^{(4)}$	0.63	2.12	1.55	2.05
MnO	n.d.	0.01	n.d.	0.02
MgO	n.d.	0.01	0.39	0.17
CaO	0.53	0.49	0.96	0.99
Na_2O	4.02	4.17	4.68	4.72
K_2O	4.25	4.24	5.09	5.02
Total	99.58	99.22	98.32	99.40

⁽¹⁾ Electron-probe analysis of a crystal-free region; ⁽²⁾ bulk analysis determined by ICP and AA; ⁽³⁾ not detected; ⁽⁴⁾ all iron as FeO.

Table 2
Summary of experimental results

sample #	T t at P _{low} ⁽¹⁾ (°C)	(sec)	ΔP (MPa)	size ⁽²⁾ (μm)	N.D. oxides ⁽³⁾	crystals ⁽⁴⁾ (cm ⁻³)
LGB-10	780	1800	100	35	2x10 ⁷	x
LGB-17	780	1200	50	45	2x10 ⁶	x
LGB-24	780	60	50	16	1x10 ⁸	x
LGB-35	780	45	5	5	2x10 ⁷	x
LGB-52	780	30	30	16	5x10 ⁶	x
LGB-58	780	300	30	12	5x10 ⁶	x
LGB-89	780	180	5	10	5x10 ⁶	x
LGB-97	780	45	30	15	4x10 ⁶	x
LGB-98	780	180	10	10	1x10 ⁷	x
LGB-104	780	30	30	20	5x10 ⁵	x x
LGB-105	780	0	0	24	3x10 ⁴	x x
LGB-124	780	5	30	10	8x10 ⁶	x
LGB-59	790	480	30	65	1x10 ⁵	x x
LGB-7	800	14400	100	250	3x10 ⁴	
LGB-16	800	900	100	280	2x10 ⁴	x
LGB-18	800	300	50	200	4x10 ⁴	x
LGB-32	800	30	5	0	0	x
LGB-34	800	30	10	0	0	x
LGB-36	800	120	5	0	0	
LGB-37	800	480	5	200	0	x
LGB-39	800	120	30	45	3x10 ³	x
LGB-53	800	1140	30	160	7x10 ³	
LGB-55	800	30	38	23	2x10 ³	x
LGB-57	800	180	30	65	7x10 ³	
LGB-84	800	180	15	27	1x10 ³	x
LGB-85	800	180	70	112	2x10 ⁴	x
LGB-88	800	5	134	36	3x10 ⁵	x
LGB-101	800	30	125	20	6x10 ⁵	
LGB-102	800	30	108	25	5x10 ⁶	
LGB-63	850	660	5	0	0	x
LGB-64	850	0	0	0	0	x
LGB-74	850	10800	30	155	4x10 ²	x
LGB-75	850	0	0	0	0	
LGB-76	850	180	30	51	6x10 ³	
LGB-81	850	180	50	70	5x10 ³	x
LGB-82	850	180	110	200	6x10 ⁵	x
LGB-83	850	180	5	0	0	x
LGB-95	850	30	135	350	3x10 ⁴	
LGB-111	850	60	120	100	1x10 ⁶	
LGB-114	850	180	100	140	4x10 ⁵	
LGB-115	850	180	90	125	2x10 ⁵	
LGB-116	850	60	115	175	7x10 ⁴	
LGB-117	850	180	106	50	1x10 ⁷	
LGB-118	850	180	88	76	2x10 ⁶	
LGB-119	850	120	115	100	1x10 ⁶	
LGB-120	850	15	115	75	6x10 ⁴	
LGB-121	850	90	114	45	1x10 ⁷	
LGB-122	850	5	115	80	6x10 ⁴	x
LGB-123	850	30	120	140	5x10 ⁵	x
LGB-125	850	7	100	40	2x10 ⁵	x
LGB-126	850	6	100	30	6x10 ⁵	
LGB-127	850	6	80	20	3x10 ⁶	
LGB-128	850	30	100	110	1x10 ⁵	
LGB-129	850	60	100	140	4x10 ⁵	x
SDC-99	800	180	30	20	3x10 ⁶	x x
SDC-103	800	60	30	15	1x10 ⁶	x x
SDC-106	815	180	30	15	1x10 ⁶	x x
SDC-107	815	180	50	25	5x10 ⁶	x x
SDC-110	850	480	30	25	2x10 ⁴	x x
SDC-113	850	0	0	55	3x10 ⁴	x x

⁽¹⁾ Time at lower pressure, not including decompression time; ⁽²⁾ based on microscopic examination (for reference only); ⁽³⁾ Fe-Ti oxides present in the sample; ⁽⁴⁾ crystals other than oxides present in the sample. In LGB samples the crystals are zircons and rare feldspars. In SDC samples the crystals include feldspar, biotite, apatite and rare amphibole, plagioclase and quartz.

microscope, or by computer processing of video images. In samples with low number densities, bubbles were counted in the whole volume of the glass. Where number densities were higher, we counted the bubbles in the area exposed to the camera at high magnification throughout the full thickness of the sample. In a few crystal-rich SDC samples, reflected light was used to count the surface distribution of the bubbles. Errors in counting may be as large as a factor of two. These large errors are mainly due to inhomogeneities in the distribution of bubbles. An extreme example is presented in Fig. 2, where there are two zones with different bubble densities. The density in the microlite-rich zone is higher by a factor of five.

3. Results

3.1. Conditions at the end of the hydration period

In order to determine the conditions in the runs just before the drop in pressure, some samples were quenched directly, with no pressure drop (Table 2). The LGB samples that were hydrated at 780°C contained bands of Fe-oxide microlites, as in the starting material, but the thin

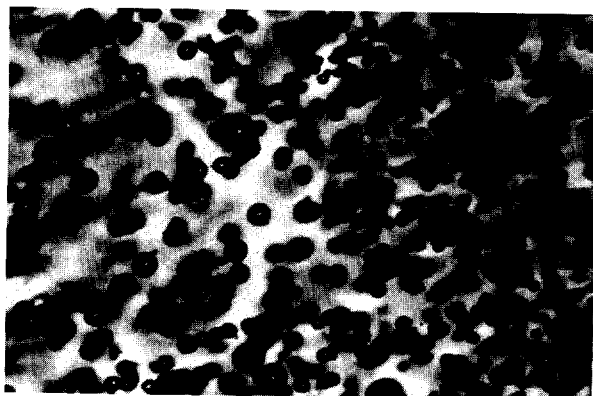


Fig. 2. LGB-58, an extreme example of the inhomogeneous distribution of bubbles. Bubble density is $2 \times 10^7 \text{ cm}^{-3}$ on the right-hand side, where oxides are abundant. On the left, where fewer oxides are present, number density is only $4 \times 10^6 \text{ cm}^{-3}$. Run time was 300 s and the lower density allowed bubbles on the left to grow more than in the denser region on the right (length = 1680 μm).

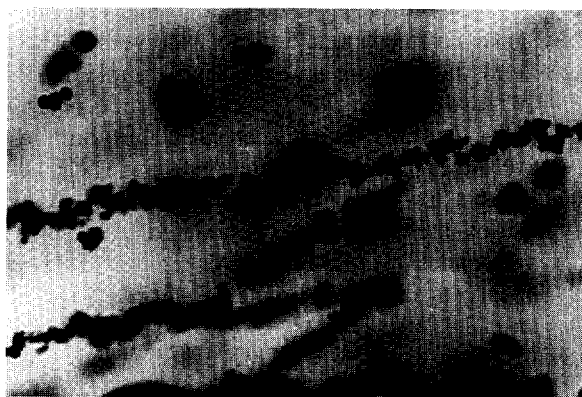


Fig. 3. LGB-35. Fe-Ti oxides and associated bubbles are all arranged along lines, following the original arrangement in the starting material. All bubbles are associated with microlites, but some microlites are free of bubbles (length = 210 μm).

narrow strings disappeared (compare Fig. 1a with the strings and Fig. 3 without them). Most iron oxides dissolved at 790°C, and they disappeared at 800°C. Only very few euhedral phenocrysts of zircon and feldspar were found at 800° and 850°C. Rare oxides were found in samples that were decompressed by more than 100 MPa. We cannot rule out the possibility that these oxides formed during decompression.

In SDC samples hydrated at temperatures up to 815°C, the amount and composition of the crystals differed little from those of the starting material. Only a small portion of the Fe-Ti oxides was dissolved, and the samples were very dark and translucent due to the large amount of oxides. In the two SDC samples run at 850°C, most of the small Fe-Ti oxides dissolved, but the larger oxides were still present, along with K-feldspar, biotite and apatite. The glass was clear and transparent. In sample SDC-110, which was run at 850°C, the Fe-Ti oxides that were not dissolved were concentrated around large biotite and feldspar crystals.

3.2. Nucleation in crystal-bearing samples

In all experiments where microlites of Fe or Fe-Ti oxides were present, bubbles were found attached to the microlites. Judging from the fol-

lowing observations, we conclude that the bubbles grew on microlites, and not vice versa:

- (1) Both the starting material and sample LGB-105 hydrated at 780°C and quenched at 150 MPa, contain many microlites, but bubbles are either rare or absent.
- (2) In the low-temperature experiments, many oxides, including those connected to bubbles, are concentrated along bands similar to those observed in the starting material (Figs. 2 and 3).
- (3) In many cases two or more bubbles are attached to a single microlite (Figs. 2 and 3) and microlites are completely surrounded by bubbles.
- (4) In a few samples, it was clear that while all bubbles are associated with microlites, many microlites are free of bubbles (Fig. 3).

The availability of microlites was the most important factor controlling bubble nucleation in these experiments. For example, in LGB-59 and LGB-104, which contain much fewer microlites than LGB-52, LGB-58, LGB-97 and LGB-124, number density is more than an order of magnitude lower, although all samples were decompressed by 30 MPa. Fig. 2 shows that where enough microlites were available (on the right-hand side), bubble densities reached a value of $2 \times 10^7 \text{ cm}^{-3}$, but on the left-hand side, where fewer microlites were present, only $4 \times 10^6 \text{ bubbles cm}^{-3}$ nucleated. Number densities are high even at low supersaturation (ΔP , the decompression after the end of hydration). For example, in LGB-35, number density reached $2 \times 10^7 \text{ cm}^{-3}$ at a ΔP of 5 MPa.

We did not attempt decompression of less than 5 MPa, but some samples indicated that modest nucleation took place at even lower decompression. In LGB-105 and SDC-113, which were quenched directly after hydration ($\Delta P = 0$), the glasses carry about $3 \times 10^4 \text{ bubbles cm}^{-3}$. It is improbable that the bubbles were formed during quenching, as the pressure in the system increased slightly during the quench. The bubbles probably nucleated during small ($< 1 \text{ MPa}$) pressure fluctuations (caused by room-temperature variations) towards the end of the hydration period. In samples LGB-35 and LGB-58 we ob-

served bimodal distributions of bubble sizes. We assume that the many small bubbles in these samples were formed in response to decompression at the end of the hydration period, while the few larger bubbles were formed earlier during the hydration period in response to pressure fluctuations. Overall, the efficiency of the Fe-Ti oxides as nucleation sites in samples where $\Delta P = 5 \text{ MPa}$ was 50–60%, in samples where $5 < \Delta P < 10 \text{ MPa}$ the efficiency was 70–90%, and in samples where $\Delta P > 30 \text{ MPa}$ it was $> 90\%$.

Nucleation rates on microlites are very high. The best estimates come from runs that were quenched shortly after decompression (e.g., LGB-124, which was decompressed to 120 MPa after 5 s). In this sample, the bubble number density in the quenched glass is $8 \times 10^6 \text{ cm}^{-3}$, yielding a minimum nucleation rate of $1.6 \times 10^6 \text{ cm}^{-3} \text{ s}^{-1}$. The actual rate might have been even higher, if all nucleation occurred in less than 5 s.

Crystal-rich SDC samples allowed us to examine the efficiency of other crystals as nucleation sites. No bubbles grew on crystals other than the Fe-Ti oxides at decompressions of less than 10 MPa (SDC-113). At larger drops in pressure, more crystals acted as nucleation sites. In sample SDC-110, crystals of biotite, feldspar, apatite and oxides existed after the hydration period. After



Fig. 4. Bubbles in contact with a biotite crystal. Note the wetting angle between the bubble–melt and the melt–crystal interfaces (Θ , see Fig. 10a). The arrow points to a bubble that wets the biotite with an obtuse angle. A sharper angle can be observed at the contact of the bubble below the biotite (LGB-110, length = $210 \mu\text{m}$).

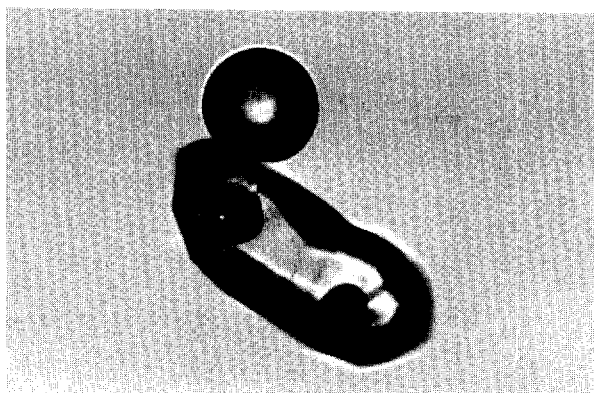


Fig. 5. A bubble in contact with a zircon. The wetting angle is small (clearly less than 40°), and the crystal is euhedral and smooth (LGB-55, length = $210\ \mu\text{m}$).

decompression by $\Delta P = 30\ \text{MPa}$ we found a high concentration of bubbles and oxides in the vicinity of the biotites and the feldspars. In the case of the biotite, it is clear that some bubbles wet its surface (Fig. 4). Bubbles were also found in contact with the edges of some apatite crystals. Bubbles that grew in the vicinity of a few of the feldspar crystals did not wet the surface of these crystals. Rather, they appear to have nucleated on neighbouring oxides. Some zircon crystals nucleated bubbles at decompressions of 30–50 MPa. In a few samples, a bubble was found attached to

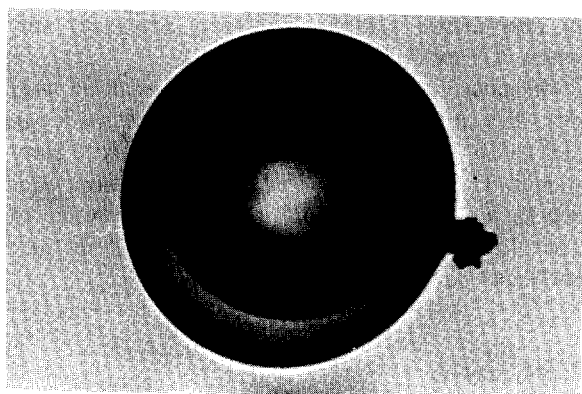


Fig. 6. A bubble in contact with an oxide microlite. The short neck, extending from the bubble to the microlite, cannot be a stable configuration, and is probably due to some shrinkage of the bubble during quenching. The wetting angle is larger than 90° (LGB-59, length = $210\ \mu\text{m}$).

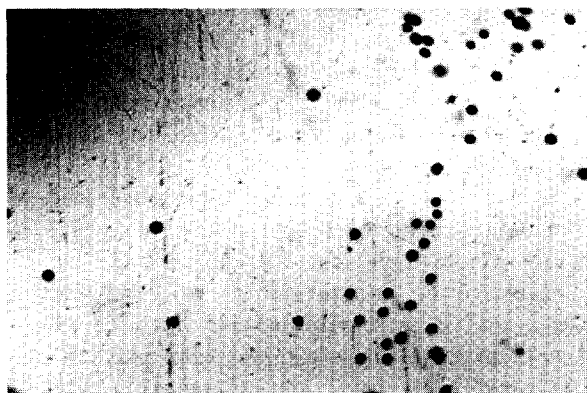


Fig. 7. LGB-76, a crystal-free sample. All bubbles are concentrated on one side of the sample, indicating that nucleation was not homogeneous (reflected light, length = $1680\ \mu\text{m}$).

a zircon crystal (Fig. 5), but other zircons in the same sample were bubble-free. Overall, about 15% of the zircons carried bubbles. In LGB-35 and LGB-59, most oxides served as nucleation sites but all zircons were bubble-free.

A crystal can act as an efficient site for heterogeneous nucleation if it can be wetted easily by the bubble, and form large bubble–crystal dihedral angles (Θ in Fig. 10). The dihedral angle formed between the bubble and the zircon is less than 40° (Fig. 5). In the case of the biotites, bubbles wet the crystal more efficiently and form angles that are larger than 90° (arrow in Fig. 4). The Fe-Ti oxides are usually smaller than the bubbles, so that the wetting angle cannot be determined. The bubble commonly completely wets one of the microlite faces. In some cases, a cylindrical neck extends from spherical bubbles towards the microlite and wets the face of the microlite with a dihedral angle of about 90° (Fig. 6).

3.3. Nucleation in crystal-free samples

No microlites have been observed in LGB samples that were heated to 800° or 850°C . Pressure drops of 15–20 MPa lead to nucleation of small numbers of bubbles ($400\text{--}7000\ \text{cm}^{-3}$). Bubble size distribution in these samples is narrow, suggesting that nucleation occurred in a single

event during decompression. The spatial distribution is not random, and in LGB-76 and LGB-81 most of the bubbles are concentrated in one zone (Fig. 7). These observations suggest that nucleation is still heterogeneous, despite the fact that no crystals were observed.

Pressure drops of 80 MPa or more lead to nucleation of large numbers of bubbles, even in LGB samples heated to 800° and 850°C (Fig. 8). Because of the large drop in pressure bubbles are large, and in extreme cases they coalesce. Number densities in these samples vary between 2×10^4 and $1 \times 10^7 \text{ cm}^{-3}$ and are on average about two orders of magnitude higher than the number densities in crystal-free samples decompressed by 15–70 MPa (Fig. 8). No correlation was found between number density and time spent at low pressure for samples decompressed by 100 and 115 MPa (Fig. 9). Moreover, both decompressions lead to similar number densities. Nucleation rates in these samples were high. The highest calculated nucleation rate of $10^5 \text{ cm}^{-3} \text{ s}^{-1}$ is shared

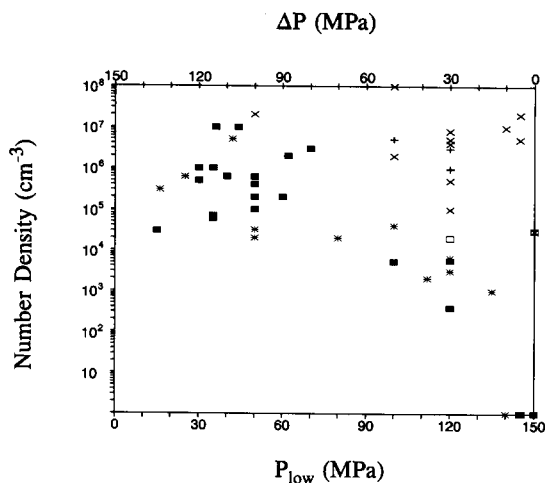


Fig. 8. Bubble number density as a function of P_{low} (pressure after decompression, bottom scale) and decompression (ΔP , top scale). ■ = LGB samples heated to 850°C; * = LGB samples heated to 800°C (both these types of LGB samples are free of microlites); × = LGB samples heated to 780° and still carrying microlites; squ = SDC samples heated to 850°C and carrying few microlites or other crystals; + = SDC samples heated to 800° and 815°C and carrying abundant microlites and crystals. Samples plotting on the bottom x-axis carry no bubbles.

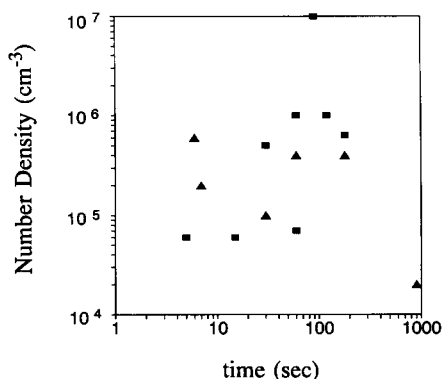


Fig. 9. Bubble number density versus time at P_{low} . ▲ = $\Delta P = 100 \text{ MPa}$; ■ = $\Delta P = 115 \text{ MPa}$.

by two samples (LGB-121 and LGB-126). The actual rate may be even higher, if nucleation took place immediately after decompression.

3.4. Summary of results

Oxide microlites are very efficient in promoting nucleation. Where present, most microlites carry bubbles even at supersaturation pressures as low as 5 MPa. In the absence of microlites, no nucleation occurs at $\Delta P < 10 \text{ MPa}$. At ΔP of about 30 MPa, some bubbles do nucleate on biotite, apatite and zircon, but nucleation is modest. Small numbers of bubbles are formed even in samples where no crystals are visible. Nucleation in crystal-free samples becomes extensive only when ΔP exceeds 80 MPa.

In microlite-bearing samples, typical number densities are about 10^7 cm^{-3} . Bubble densities of 10^5 to 10^7 cm^{-3} are reached in crystal-free samples, but only at $\Delta P > 80 \text{ MPa}$. Nucleation rates are faster than $10^5 \text{ cm}^{-3} \text{ s}^{-1}$ in the absence of microlites and faster than $10^6 \text{ cm}^{-3} \text{ s}^{-1}$ in their presence.

4. Discussion

4.1. Nucleation theory

When a melt becomes supersaturated, the excess dissolved water must eventually separate and

form a vapour phase. According to classical nucleation theory [8,23–25], the process starts with the formation of small clusters of water molecules, due to local fluctuations in the concentration of molecular water in the melt. These clusters, or nuclei, may either grow or dissolve by diffusion of water molecules. The new vapour phase has a lower bulk free energy than the supersaturated melt, but the formation of an interface consumes energy, and tends to destabilize the cluster. The growing cluster takes on a spherical shape in order to minimize surface energy. It grows until it reaches a critical size. At this size, the energy released when an additional water molecule enters the volume of the cluster balances the increase in surface area and surface energy. Further addition of water molecules to the nucleus leads to a decrease in the energy of the melt–bubble system, and this stable nucleus can continue its spontaneous growth. The critical radius is:

$$r^* = 2\sigma / (P^* - P) \quad (1)$$

where σ is the surface tension, P^* the internal pressure in the nucleus when in equilibrium with the supersaturated melt, and P is the ambient pressure in the melt. The energy it takes to form the critical nucleus can be calculated by integrating the contributions of the volume and surface energies involved in the growth of the nucleus until the latter reaches the critical size [8,24]:

$$\Delta F^* = 16\pi\sigma^3 / 3\Delta P^2 = A^*\sigma / 3 = V^*\Delta P / 2 \quad (2)$$

where ΔF^* is the Helmholtz free energy for the formation of critical nuclei, or the activation energy for nucleation, $\Delta P = P^* - P$ is the supersaturation pressure, and A^* and V^* are the surface area and the volume of the critical nucleus. Note that the activation energy is not constant, and varies with supersaturation. During the ascent of a saturated melt, P (the ambient pressure) decreases, but P^* (the equilibrium vapour pressure of the melt) remains relatively constant. As ΔP increases, ΔF^* decreases, until it is of the order of kT and nucleation becomes rapid. More ex-

plicitly, the nucleation rate (J) can be estimated following Hirth et al. [24]:

$$J = J_0 \exp[-\Delta F/kT] = 2n_0^2 V_m D (\sigma/kT)^{1/2} / a_0 \exp[-16\pi\sigma^3 / 3kT\Delta P^2] \quad (3)$$

where k is Boltzman's constant, T is temperature, and n_0 is the concentration of nucleation sites, which in the case of bubble nucleation from the melt is the concentration of dissolved water molecules. V_m is the volume of a water molecule in the melt, D is the diffusion coefficient of molecular water in rhyolite, and a_0 is the distance between two sites of water molecules in the melt. The derivation of the expression for J_0 is given in the appendix.

Eq. (3) may be used to estimate the supersaturation (ΔP) required for a given nucleation rate. The major source of uncertainty is the value of the surface tension (σ). The only relevant data are those of Epel'baum et al. [26], who determined $\sigma = 0.072$ and 0.061 N/m for Rapakivi granite with 4.48 and 5.71 wt% water respectively. Using $\sigma = 0.06$ N/m, $n_0 = 3 \times 10^{28} \text{ cm}^{-3}$ and $a_0 = 7\text{\AA}$ (corresponding to 3.5 wt% molecular water, or 5 wt% total water in the melt), $D = 5.45 \times 10^{-12} \text{ m}^2/\text{s}$ [20] and V_m corresponding to molecular radius of 1.4\AA [20] we obtain $J_0 = 3 \times 10^{27} \text{ cm}^{-3} \text{ s}^{-1}$. Using Eq. (3), we calculate that a slow nucleation rate of $1 \text{ cm}^{-3} \text{ s}^{-1}$ requires a ΔP of 61 MPa. Rates in excess of $10^4 \text{ cm}^{-3} \text{ s}^{-1}$, which are regarded as instantaneous [3,23], are attained at $\Delta P > 66$ MPa. These supersaturations are very high and mean that melts saturated at 5 km (~ 5 wt% total water) must ascend by about 2 km before bubbles can nucleate homogeneously.

The supersaturation required for heterogeneous nucleation may be much lower than in the case of homogeneous nucleation. In the presence of crystals, the activation energy decreases by a factor ϕ due to the decrease in surface energy [8]:

$$\Delta F = 16\pi\sigma^3\phi / 3\Delta P^2 \quad (4)$$

$$\phi = (2 - \cos \Theta)(1 + \cos \Theta)^2 / 4 \quad (5)$$

$$\cos \Theta = (\sigma_{cv} - \sigma_{cm}) / \sigma_{mv} \quad (6)$$

$\sigma_{mv} = \sigma$ is the surface energy of the melt–vapour interface, and ‘c’ in the subscripts stands for crystal (Fig. 10a). If the melt wets the surface completely, $\Theta = 0$ and $\phi = 1$, and the crystal does not ease the nucleation. If the vapour wets the crystal completely, $\Theta = 180^\circ$ and $\phi = 0$ and no supersaturation is needed. If the vapour and melt equally wet the surface of the crystal $\Theta = 90^\circ$ and $\phi = 0.5$, and ΔP can be smaller by a factor of $\sqrt{2}$ and still yield the same value of ΔF^* as in homogeneous nucleation. Fig. 11 shows the decrease in ΔP required for nucleation as a function of increasing Θ (and ϕ). It can be seen that Θ in excess of 150° is needed in order to impose a substantial decrease in ΔP . Moreover, since n_0 is smaller in the case of heterogeneous nucleation (nucleation sites are only around the crystals), a somewhat larger Θ is needed.

A further decrease in the required supersaturation may be achieved if the crystal surface is rough. Sigbee [27] has shown that the presence of a 90° corner facilitates nucleation. If the wetting angle exceeds 135° (which means a flat interface between the bubble and the melt) no activation is necessary (Figs. 10b and 11).

4.2. Heterogeneous nucleation on crystals

The wetting angle of the crystals and crystal morphology are critical parameters in determining the efficiency of crystals as nucleation sites. Our experimental results show that in the presence of suitable crystals heterogeneous nucleation occurs at low supersaturation. Nucleation is

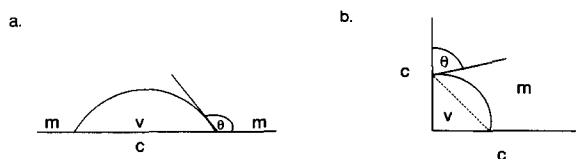


Fig. 10. Wetting angles. (a) Bubble on a smooth surface. m = melt; v = vapour; c = crystal. The dihedral wetting angle, Θ , is measured through the melt from the melt–crystal interface to the tangent to the bubble–crystal interface. (b) Bubble in a corner. Note that when Θ reaches 135° , a flat interface is formed between bubble and melt (dashed line), bubble radius is infinite, $P^* = P$, and no activation energy is needed for the formation of a nucleus.

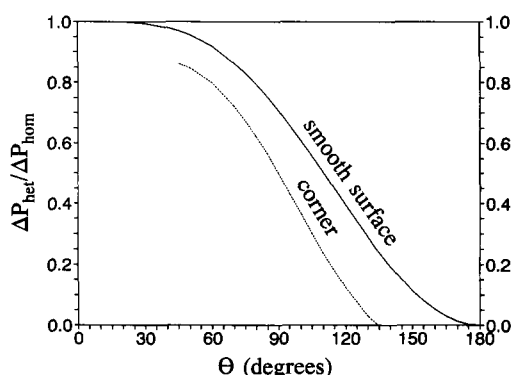


Fig. 11. Required supersaturation for constant ΔF versus the wetting angle Θ . Solid line = smooth surface. When $\Theta = 0$, ΔP is that needed for the onset of homogeneous nucleation. For other values of Θ , $\Delta P_{het}/\Delta P_{hom}$ behaves as $(\phi)^{1/2}$. Dashed line = nucleation on a corner (after [27]).

very fast, and nucleation rates are mainly controlled by the number of available sites. We base this conclusion on the following observations (described in detail in section 3.2):

- (1) The number densities of bubbles in samples containing oxides are always higher than in oxide-free samples decompressed by a comparable amount (Fig. 8).
- (2) The narrow distribution of bubble sizes found in most samples.
- (3) In samples containing many crystals, almost all bubbles are attached to the crystals.

We found Fe-Ti oxides to be most efficient as nucleation sites. Supersaturation of the order of 1 MPa was sufficient to initiate some nucleation in sample SDC-113, and most microlites carried bubbles at $\Delta P = 5$ MPa (LGB-35 and LGB-89). Combining Eq. (3), (4) and (5) we can calculate the necessary Θ for obtaining nucleation rates of $J = 1$ bubble/microlite/s at $\Delta P = 5$ MPa. In this case the number of sites on a $5 \mu\text{m}$ microlite is $n_0^{\text{microlite}} = n_0 a_0 4\pi R^2 = 1.6 \times 10^8$ molecules. If the other parameters in Eq. (3) are kept as above, we obtain $\phi = 3.5 \times 10^{-3}$ and $\Theta = 158.5^\circ$. Because of their small size, most microlites are wetted from edge to edge and Θ cannot be determined. The necked bubbles (Fig. 6) as well as some very small bubbles attached to microlites do suggest that Θ is greater than 90° , but is clearly smaller than 158° . The neck itself cannot be a stable configura-

tion and was probably formed due to a decrease in the bubble volume during quenching. In any case, neck formation clearly shows that during its shrinkage the bubble adheres to the microlite better than to the melt, suggesting that $\sigma_{cv} < \sigma_{cm}$ and $\Theta > 90^\circ$.

While Θ is not large enough to explain the extensive nucleation on smooth surfaces, such large angles can be very efficient when nucleation takes place on corners. As shown in the previous section, $\Theta = 135^\circ$ is sufficient to eliminate the activation energy for nucleation at corners of 90° . The rough morphology of the microlites provides many such corners and may be the reason for their efficiency as sites.

Our data for nucleation on other crystals are somewhat limited, since their abundance is much lower. No other phase was as effective as the oxide microlites. Some bubbles were found on biotites (Fig. 4). These formed large angles ($\Theta \approx 120^\circ$), which together with the platy nature of biotite may explain the formation of bubbles on corners at $\Delta P = 30$ MPa (Fig. 5). Only a few apatite and zircon crystals were found associated with bubbles in experiments with ΔP of 10–50 MPa (most were bubble-free). Rare feldspar and quartz crystals found in the SDC samples were not observed in contact with bubbles. Bubbles grew very close to the feldspar grains, but never wetted their surface. A similar situation can be seen in a dacite sample from Mount St. Helens (fig. 1 of [28]) where the wetting angles between bubbles and plagioclase crystals (Θ) are lower than 20° . More experiments are necessary to substantiate this negative conclusion. If this conclusion is founded, it implies that crystallization of some minerals, such as feldspar, can produce large supersaturation pressures in cooling magma chambers, without initiating nucleation.

4.3. Nucleation in crystal-free melts

Samples of LGB rhyolite heated to temperatures of 800°C or higher lost all their crystals, except for rare zircon or feldspar crystals. At $\Delta P < 10$ MPa, no bubbles were formed (Fig. 8). At $15 < \Delta P < 70$ only a small number of bubbles were formed ($400\text{--}40,000$ bubbles cm^{-3}). The

non-uniform spatial distribution (Fig. 7) and the narrow size distribution in these experiments indicate that nucleation was not homogeneous, even though no crystals were observed. When ΔP exceeded 80 MPa, the number density of bubbles increased sharply and most samples carried more than 10^5 bubbles cm^{-3} .

Can the increase in number density at $\Delta P \approx 80$ be attributed to crossing the threshold for homogeneous nucleation at that pressure? On the one hand, this threshold is very close to the calculated value of 66 MPa (section 4.1). On the other, the number density correlates with neither ΔP nor the time spent at low pressure (Fig. 9). The similar bubble densities found in experiments with ΔP of 100–130 MPa (Table 2) contrast with the prediction of classical nucleation theory. According to Eq. (3) the rate of homogeneous nucleation at $\Delta P = 130$ MPa must exceed that at 100 MPa by many orders of magnitude. If homogeneous nucleation produced 6×10^4 bubbles in 5 s after 115 MPa decompression in LGB-122, a longer period should have led to higher number densities. This was not the case in LGB-120 (15 s) and LGB-116 (60 s). The number density did not increase even though the average separation between the bubbles (~ 250 μm) allowed further nucleation.

The absence of correlation discussed above may be understood easily if nucleation was not homogeneous. In this case, the number density is controlled simply by the number of sites. At large decompressions, new and more abundant sites become operative, allowing many more bubbles to be formed. We note that the large number and large size of bubbles in most high-decompression runs makes it difficult to determine the absence of crystals and to measure the size distribution of the bubbles. Thus, at present, we cannot exclude the possibility that nucleation was homogeneous in some of the runs.

5. Geological implications

The experimental data that we present here indicate that the presence or absence of efficient nucleation sites can lead to two distinct modes of

bubble formation. When a large number of efficient sites (e.g., Fe-Ti oxides) are present, bubble nucleation requires very small supersaturation, and, to a good approximation, gas and magma are in equilibrium. In magmas that are crystal-free or contain crystals that are inefficient at nucleating bubbles, very high degrees of supersaturation are required in order to initiate nucleation. This mode is similar to the “disequilibrium” degassing of Stasiuk et al. [29].

In the presence of efficient sites, the low supersaturation required for bubble nucleation may be easily attained in an ascending current of a convecting magma chamber. If the magma is saturated, or only slightly undersaturated, at the bottom of the chamber, pressure decrease during ascent may be sufficient for initiating bubble nucleation. Bubble formation leads to a substantial density decrease in the ascending magma and to increased ascent rates. When no efficient crystals are present, the higher required degrees of supersaturation are very difficult to reach during convection. Thus, the appearance of oxides, or other efficient sites, may alter the style of convection in silicic chambers.

In a crystallizing magma chamber the order of crystallization may lead to contrasting modes of evolution. During crystallization the concentration of dissolved water increases [30,31] and eventually reaches saturation. If sufficient amounts of efficient crystals are present when water saturation is achieved, bubbles nucleate and grow continuously and pressure in the chamber rises gradually [2]. If the crystallizing phases are inefficient nucleation sites (as may be the case for feldspars), crystallization proceeds past the saturation concentration until supersaturation is high enough for nucleation on the crystals present, or until a more efficient phase joins the crystallizing assemblage. In this case, the growth of bubbles will be rapid [32] and pressure within the chamber will rise quickly. This may leave a short time interval between inflation of the chamber and eruption.

The phenocryst assemblage in the magma is also important for degassing in the volcanic conduit. The presence of efficient sites ensures equilibrium degassing. As the magma rises in the conduit, the confining pressure drops. When the

latter falls below the saturation pressure, bubbles nucleate. In this case, the interval between the depth of exsolution (where bubbles first appear) and the depth of fragmentation (where the bubble walls collapse) is large (see [1] for further details). This large interval allows a larger distance over which gas may be lost to the wallrock [33,34]. If no efficient sites are available, bubbles nucleate only higher in the column. The growth of bubbles is much faster [32], and the depth interval over which gas may be lost to the wallrock is much smaller.

6. Conclusions

(1) In crystal-free samples no nucleation takes place at $\Delta P < 10$ MPa, modest nucleation takes place at $15 > \Delta P > 70$ MPa, and vast amounts of nucleation take place at $\Delta P > 80$ MPa. Our observations suggest that in all cases nucleation of bubbles was not homogeneous.

(2) Some crystals were more efficient than others as sites for heterogeneous nucleation. The efficiency mainly depends on surface tension (as reflected in the wetting angles), but crystal morphology is also important.

(3) Oxide microlites serve as very efficient sites. Nucleation commenced with decompressions of less than 1 MPa. As many as 10^6 – 10^8 bubbles cm^{-3} were formed at decompressions of $\Delta P \geq 5$ MPa. The bubbles were formed less than 5 s after decompression. The high efficiency may be explained by the low surface tension of the microlite–bubble interface and the rough morphology of the crystals.

(4) Bubbles grew on biotite, zircon and apatite at $\Delta P = 30$ MPa. No bubbles were associated with the rare feldspar or quartz crystals. More experiments are necessary to substantiate this negative conclusion.

(5) Equilibrium degassing requires the presence of a sufficient number of crystals with high nucleation efficiency. In the absence of such sites, high supersaturation levels may be attained in a crystallizing magma chamber. These two modes of degassing may lead to contrasting styles of convection, pressure build-up and eruption.

Acknowledgements

We thank Ed Stolper for his advice and encouragement throughout the course of this study. We also thank David Szafrank for the EPMA analysis, Ronit Kessel for the ICP, and Phil Ihinger and Jen Blank for the samples. Yehoshua Kolodny, Steve Sparks, Yan Bottinga and an anonymous reviewer made valuable comments on the paper. Funding was provided by the Israel–USA Binational Science Foundation.

Appendix A: Derivation of the pre-exponential term in the rate equation (Eq. 3)

The value of the pre-exponential factor in Eq. (3) is not well constrained by classical nucleation theory. However, current estimates lead to very large values that should not be ignored [23,24]. Here we follow, with some modification, the derivation of Hirth et al. [24]:

$$J_0 = n_0 \beta Z \quad (\text{A1})$$

where n_0 is the concentration of nucleation sites, which in the case of water bubbles nucleating from the melt is the concentration of dissolved water molecules, β is the growth frequency of clusters across the critical size (s^{-1}), and Z is the Zeldovitch factor, which corrects for the fact that the growth process is actually accruing at a steady state rather than at equilibrium.

The growth frequency (β) is controlled by water diffusion across the interface:

$$\beta = 4\pi r^{*2} n_s \nu_0 \exp(-\Delta F_d/kT) \quad (\text{A2})$$

where n_s is the surface concentration of water molecules, ν_0 is the jump frequency for diffusion and ΔF_d is the activation energy for diffusion. The diffusion coefficient of H_2O can be expressed as

$$D = a_0^2 N_v \nu_0 \exp(-\Delta F_d/kT)$$

[35] where a_0 is the distance between two sites of water molecules in the melt and N_v is the frac-

tion of free sites ($N_v \approx 1$). Estimating $n_s = n_0 a_0$, we obtain:

$$\beta = 4\pi r^{*2} n_0 D / a_0 \quad (\text{A3})$$

It should be noted that in systems that are not isothermal the exponential part of D should be added to the activation exponent when β is combined into the rate expression, and only D_0 , the pre-exponential term, should be included in J_0 [10]. The Zeldovitch factor is:

$$Z = (3\Delta F^* V_m^2 / 16\pi^3 k T r^{*6})^{1/2} \\ = (\sigma/kT)^{1/2} V_m / 2\pi r^{*2} \quad (\text{A4})$$

where V_m is the volume of a water molecule in the melt, r^* is the radius of the critical nucleus and ΔF^* is the free energy of formation for that nucleus (Eq. 2). Combining (A1), (A3) and (A4), the pre-exponential term can be written:

$$J_0 = 2n_0^2 V_m D (\sigma/kT)^{1/2} / a_0 \quad (\text{A5})$$

The calculated value is $3 \times 10^{27} \text{ cm}^{-3} \text{ s}^{-1}$ (see text).

References

- [1] L. Wilson, R.S.J. Sparks and G.P.L. Walker, Explosive volcanic eruptions—IV. The control of magma properties and conduit geometry on eruption column behavior, *Geophys. J.R. Astron. Soc.* 63, 117–148, 1980.
- [2] S. Tait, C. Jaupart and S. Vergnolle, Pressure, gas content and eruption periodicity of a shallow, crystallizing magma chamber, *Earth Planet. Sci. Lett.* 92, 107–123, 1989.
- [3] R.S.J. Sparks, The dynamics of bubble formation and growth in magmas: a review and analysis, *J. Volcanol. Geotherm. Res.* 3, 1–37, 1978.
- [4] B.F. Houghton and C.J.N. Wilson, A vesicularity index for pyroclastic deposits, *Bull. Volcanol.* 51, 451–462.
- [5] S. Newman, S. Epstein and E.M. Stolper, Water, carbon dioxide and hydrogen isotopes in glasses from the ca. 1340 A.D. eruption of the Mono craters, California: Constraints on degassing phenomena and initial volatile content, *J. Volcanol. Geotherm. Res.* 35, 75–96, 1988.
- [6] A.T. Anderson, S. Newman, S.N. Williams, T.H. Druitt, C. Skirius and E. Stolper, H_2O , CO_2 , Cl and gas in Plinian and ash-flow Bishop Rhyolite, *Geology* 17, 221–225, 1989.

- [7] N.W. Dunbar and P.R. Kyle, Volatile contents of obsidian clasts in tephra from the Taupo volcanic zone, New Zealand: Implications for eruptive processes, *J. Volcanol. Geotherm. Res.* 49, 127–145, 1992.
- [8] L.D. Landau and E.M. Lifshitz, *Statistical Physics*, Pergamon, New York, 1980.
- [9] A. Toramaru, Vesiculation process and bubble size distribution in ascending magmas with constant velocities, *J. Geophys. Res.* 94, 17523–17542, 1989.
- [10] Y. Bottinga and M. Javoy, MORB degassing: Bubble nucleation, *J. Geophys. Res.* 95, 5125–5131, 1990.
- [11] A. Toramaru, Measurement of bubble size distribution in vesiculated rocks with implications for quantitative estimation of eruption process, *J. Volcanol. Geotherm. Res.* 43, 71–90, 1990.
- [12] M.T. Mangan, K.V. Cashman and S. Newman, Vesiculation of basaltic magma during eruption, *Geology* 21, 157–160, 1993.
- [13] A.C. Zettlemoyer, ed., *Nucleation*, Dekker, New York, 1969.
- [14] W.R. Wilcox and V.H.S. Kuo, Gas bubble nucleation during crystallization, *J. Crystal Growth* 19, 221–228, 1973.
- [15] G.M. Pound and D. Robertson, Selected values of critical supersaturation for nucleation from the vapor of crystals on substrates, in: *Preparation and Properties of Solid State Materials*, W.R. Wilcox and R.A. Lefever, eds., pp. 123–131, Dekker, New York, 1977.
- [16] M. Blander, Bubble nucleation in liquids, *Adv. Colloid Interface Sci.* 10, 1–32, 1979.
- [17] T. Murase and A. McBirney, Properties of some common igneous rocks and their melts at high temperatures, *Geol. Soc. Am. Bull.* 84, 3536–3592, 1973.
- [18] N.S. Bagdassarov and D.B. Dingwell, Deformation of foamed rhyolites under internal and external stresses: an experimental investigation. *Bull. Volcanol.* 55, 147–154, 1993.
- [19] P.D. Ihinger, An experimental study of the interaction of water with granitic melt, Ph.D. Thesis, California Inst. Technol., Pasadena, 1991.
- [20] Y. Zhang, E.M. Stolper and G.J. Wasserburg, Diffusion of water in rhyolitic glasses, *Geochim. Cosmochim. Acta* 55, 441–456, 1991.
- [21] S. Newman, E.M. Stolper and S. Epstein, Measurement of water in rhyolitic glasses: Calibration of an infrared spectroscopic technique, *Am. Mineral.* 71, 1527–1541, 1986.
- [22] L.A. Silver, P.D. Ihinger and E. Stolper, The influence of bulk composition on the speciation of water in silicate glasses, *Contrib. Mineral. Petrol.* 104, 142–162, 1990.
- [23] W.J. Dunning, General and theoretical introduction, in: *Nucleation*, A.C. Zettlemoyer, ed., pp. 1–67, Dekker, New York, 1969.
- [24] J.P. Hirth, G.M. Pound and G.R. St. Pierre, Bubble nucleation, *Metall. Trans.* 1, 939–945, 1970.
- [25] L.A. Swagner and W.C. Rhines, On the necessary conditions for homogeneous nucleation of gas bubbles in liquids, *J. Crystal Growth* 12, 323–326, 1972.
- [26] M.B. Epel'baum, I.V. Bababashov and T.P. Salova, Surface tension of felsic magmatic melts at high temperatures and pressures, *Geokhimiya* 3, 461–464, 1973.
- [27] R.A. Sigbee, Vapor to condensed phase heterogeneous nucleation, in: *Nucleation*, A.C. Zettlemoyer, ed., pp. 151–224, Dekker, New York, 1969.
- [28] J.C. Eichelberger and D.B. Hayes, Magmatic model for the mount St. Helens blast of May 18, 1980, *J. Geophys. Res.* 87, 7727–7738, 1982.
- [29] M.V. Stasiuk, C. Jaupart and R.S.J. Sparks, On the variations of flow rate in non-explosive lava eruptions, *Earth Planet. Sci. Lett.* 114, 505–516, 1993.
- [30] C.W. Burnham, The importance of volatile constituents, in: *The Evolution of Igneous Rocks: Fiftieth Anniversary Perspectives*, H.S. Yoder, Jr., ed., pp. 439–482, Princeton University Press, Princeton, 1979.
- [31] S. Blake, Volatile oversaturation during the evolution of silicic magma chambers as an eruption trigger, *J. Geophys. Res.* 89, 8237–8244, 1984.
- [32] A.A. Proussevitch, D.L. Sahagian and A.T. Anderson, Dynamics of diffusive bubble growth in magmas: isothermal case, *J. Geophys. Res.* 98, 22283–22307, 1993.
- [33] J.C. Eichelberger, C.R. Carrigan, H.R. Westrich and R.H. Price, Non-explosive silicic volcanism, *Nature* 323, 598–602, 1986.
- [34] C. Jaupart and C. Allegre, Gas content, eruption rate and instabilities of eruption regime in silicic volcanoes, *Earth Planet. Sci. Lett.* 102, 413–429, 1991.
- [35] J. Frenkel, *The Kinetic Theory of Liquids*, New York, 1955.